Research Article Vol. 28, No. 14 / 6 July 2020 / Optics Express 20379
Optics EXPRESS

Agile frequency transformations for dense wavelength-multiplexed communications

HSUAN-HAO LU,[1] BING QI,[2,3] BRIAN P. WILLIAMS,[2] PAVEL LOUGOVSKI,[2] ANDREW M. WEINER,[1] AND JOSEPH M. LUKENS[2,*]

[1] *School of Electrical and Computer Engineering and Purdue Quantum Science and Engineering Institute, Purdue University, West Lafayette, Indiana 47907, USA*
[2] *Quantum Information Science Group, Computational Sciences and Engineering Division, Oak Ridge National Laboratory, Oak Ridge, Tennessee 37831, USA*
[3] *Department of Physics and Astronomy, University of Tennessee, Knoxville, Tennessee 37996, USA*
[*] *lukensjm@ornl.gov*

Abstract: The broad bandwidth and spectral efficiency of photonics has facilitated unparalleled speeds in long-distance lightwave communication. Yet efficient routing and control of photonic information without optical-to-electrical conversion remains an ongoing research challenge. Here, we demonstrate a practical approach for dynamically transforming the carrier frequencies of dense wavelength-division–multiplexed data. Combining phase modulators and pulse shapers into an all-optical frequency processor, we realize both cyclic channel hopping and 1-to-N broadcasting of input data streams for systems with $N = 2$ and $N = 3$ users. Our method involves no optical-to-electrical conversion and enables low-noise, reconfigurable routing of fiber-optic signals with in principle arbitrary wavelength operations in a single platform, offering new potential for low-latency all-optical networking.

1. Introduction

All-optical signal processing provides intriguing opportunities for next-generation data communication and logic, with the possibility to surpass electronics in speed, latency, and energy efficiency [1,2]. A variety of proof-of-principle experiments based on nonlinear-optical interactions [3,4] have demonstrated foundational capabilities, including high-speed photonic logic [5,6], tunable delay lines [7,8], and wavelength exchange [9] and multicasting [10,11]. Nevertheless, solutions based on optical nonlinearities possess undesirable features, such as the need for strong pump fields and limited prospects for reconfigurability in a single system, given that the variety of functionalities demonstrated so far are based on distinct photonic components. Recently [12], we investigated a hybrid processing approach based on electro-optic phase modulators (EOMs) and pulse shapers—dubbed the "all-optical frequency processor" (AFP)—in which the control is accomplished by electrical signals, but the operations preserve the data carriers entirely in the optical domain. Here we leverage these theoretical results and experimentally demonstrate agile frequency operations on wavelength-division–multiplexed (WDM) data streams. Utilizing a three-element AFP, we realize channel hopping and broadcasting of binary phase-shift keyed (BPSK) signals for up to three users in 25 GHz WDM channels in the same fiber. Our results extend the reach of EOM/pulse-shaper frequency operations beyond narrowband quantum frequency modes [13–17] to modulated classical data, providing a new route toward low-latency, reconfigurable, and high-capacity all-optical networking.

#396142 https://doi.org/10.1364/OE.396142
Journal © 2020 Received 24 Apr 2020; revised 4 Jun 2020; accepted 9 Jun 2020; published 24 Jun 2020

Optics EXPRESS

2. Background

Consider a comb of WDM carriers spaced by frequency $\Delta\omega$: $\omega_n = \omega_0 + n\Delta\omega$ ($n \in \mathbb{Z}$), each with a baseband data stream described by complex amplitude $a_n(t)$. The AFP ideally acts as a complex matrix V_{mn} relating input signals $a_n(t)$ to output signals $b_m(t)$ according to $b_m(t) = \sum_n V_{mn} a_n(t)$ [12,13]. Specifically, an EOM applying a $\frac{2\pi}{\Delta\omega}$-periodic phase modulation pattern $\varphi(t)$ relates the total input field $E_{\text{in}}(t) = \sum_n a_n(t)e^{-i\omega_n t}$ to the output $E_{\text{out}}(t) = \sum_n b_n(t)e^{-i\omega_n t}$ according to $E_{\text{out}}(t) = e^{i\varphi(t)}E_{\text{in}}(t)$ so that, equating frequency components, we have

$$b_m(t) = \sum_{n=-\infty}^{\infty} c_{m-n} a_n(t), \tag{1}$$

where $c_k = \frac{\Delta\omega}{2\pi}\int_0^{\frac{2\pi}{\Delta\omega}} dt\, e^{i\varphi(t)} e^{ik\Delta\omega t}$ are the Fourier series coefficients of the EOM transformation. In this form we see clearly the EOM's function as a multimode interferometer, mixing and combining inputs in each channel in a generally nontrivial fashion. On the other hand, the pulse shaper applies an arbitrary phase shift to each channel, so that $E_{\text{out}}(t) = \sum_n e^{i\phi_n} a_n(t) e^{-i\omega_n t}$, or

$$b_n(t) = e^{i\phi_n} a_n(t). \tag{2}$$

Physically, this requires pulse shaper resolution sufficiently fine so that phase-to-amplitude conversion at the transitions between adjacent channels does not modify the data streams. For example, if we define a guard band $\Delta\omega_G$ centered at each channel edge $\omega_n + \frac{\Delta\omega}{2}$, the full modulation bandwidth $\Delta\omega_{\text{mod}}$ of an optical carrier must satisfy $\Delta\omega_{\text{mod}} < \Delta\omega - \Delta\omega_G$ for the proposed model to hold.

The complete operation resulting from a cascade of EOM and pulse shaper elements follows by successively taking the output b_n from each component [Eq. (1) or (2)] and placing it into input position a_n of the next, with the relevant constants c_k or ϕ_n determined by the settings of each device. As formally presented, this model involves a countably infinite number of frequency modes, ill-suited for numerical implementation. Accordingly, we instead discretize each temporal period into M samples ($M \gg N$)—equivalent to truncating to M frequency channels—and represent the overall transformation as an $M \times M$ matrix of factors, with each EOM acting as a diagonal unitary in *time* and each pulse shaper as a diagonal unitary in *frequency*. Consequently, the complex mode-transformation matrix V_{mn} relating the input field at channel n to output channel m for our three-element AFP can be described as:

$$V = (FD_{\text{EOM}_2}F^\dagger)D_{\text{PS}}(FD_{\text{EOM}_1}F^\dagger), \tag{3}$$

where D_{EOM_1} and D_{EOM_2} (D_{PS}) represent the diagonal transformations of the EOMs (pulse shaper) in discrete time (frequency), and F is the $M \times M$ discrete Fourier transform (DFT) matrix, used in this context to approximate the continuous Fourier transform between temporal and spectral representations. (Larger AFPs follow from incorporating additional factors in the above.) Provided M is sufficiently large to prevent aliasing at the edges of the frequency-channel space (we use $M = 128$), this model provides an accurate approximation to the physical transformation around the N frequency channels of interest ($\omega_n = \omega_0 + n\Delta\omega; n = 0, 1, \ldots, N-1$). The objective then is to find the EOM and pulse shaper settings implementing a transformation matrix V that matches the desired operation.

The general problem of optimizing EOM and pulse shaper configurations to synthesize frequency-mode operations has been explored in detail in the context of quantum information processing with frequency-encoded photons [13–17]. However, the case of classical communications entails key differences in the design. For one, the typical metrics for quantifying a quantum-optical operation—e.g., fidelity and success probability—prove less meaningful in the classical context, where one is ultimately interested in symbol recognition. Additionally, whereas

Optics EXPRESS

the deadtime and jitter of single-photon detectors limit typical quantum information transmission rates to much lower than the channel spacings in dense WDM, modern classical communication systems achieve modulation bandwidths approaching the channel spacings themselves. We address both of these differences through (i) use of SNR as design metric and (ii) consideration of GHz-rate modulated data.

Figure 1 offers a concept of our AFP and the operations we consider. The AFP consists of two EOMs, separated by a pulse shaper. Surrounding the AFP are example input spectra transforming through the system, for a three-channel broadcast operation (top) and two-channel cyclic hop (bottom). Each user encodes the data stream on a predefined wavelength channel (step I). The first EOM generates sidebands spreading the inputs into adjacent frequency channels (step II); then the phase applied by the central pulse shaper, coupled with the second EOM, returns the optical energy into the original channel subspace (step III), having undergone the desired transformation (either broadcast or cyclic hop; see the corresponding EOM/pulse-shaper configurations in Appendix A.1). Importantly, while the AFP settings are different between the top and bottom cases, they are fixed independently of the input; that is, the AFP will broadcast or frequency-hop the input data for any channel within the network. This condition distinguishes our approach from other recent work on EOM/dispersion-based data transformations, where the symbols for multiple data streams are generated *in situ* by the same EOMs which perform temporal shaping and define the frequency carriers [18]. The AFP paradigm, by contrast, focuses on routing arbitrary inputs with a particular transformation, so that the control parameters are independent of the incoming fields and specific data format.

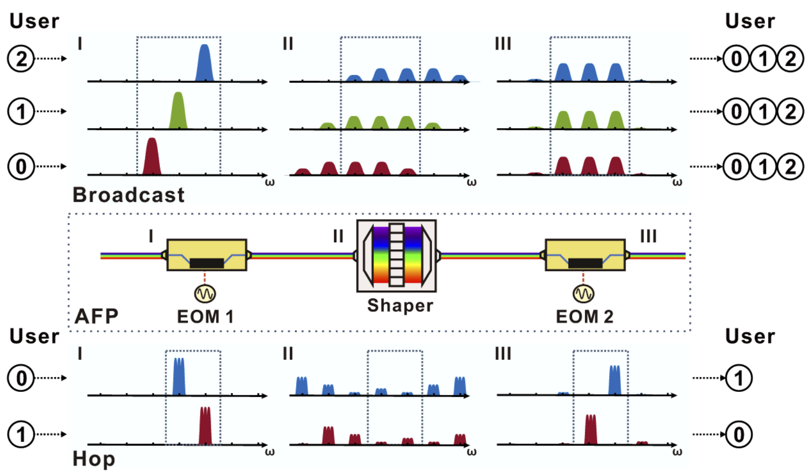

Fig. 1. Example transformations for three-user broadcast (top) and two-user hop (bottom) on our three-element AFP. Dashed boxes enclose the channels of interest in our WDM network, and each user $n \in \{0, 1, 2\}$ is associated with a particular channel frequency ω_n. The intensity distribution at each step matches the transformations implemented experimentally (see Appendix A.2).

3. Experiment design

We utilize the setup in Fig. 2 for testing. A single-frequency C-band laser is split into two paths: 5 mW is sent to an optical hybrid to serve as the local oscillator (LO), and the remainder to EOM A to generate the data carriers, spaced at 25 GHz (this comb generator need not be phase coherent with the AFP). EOM B applies BPSK data at 1 Gb/s to all carriers simultaneously. A pulse shaper equalizes channel amplitudes and sends them through different fiber paths, with

Optics EXPRESS

differential delays chosen to exceed the 1 ns bit period and decorrelate the data and randomize the relative phase, thus emulating independent channels. After wavelength multiplexing, all carriers pass through the AFP, undergoing either the broadcast or hop operation; the output mixes with the LO on a conjugate homodyne detector, consisting of a 90° optical hybrid and two balanced detectors. We record X and Y outputs at 20 GS/s and take one sample per 1 ns period as the symbol value; this condition defines the effective "symbol pulse" for calibration. Digital phase correction is performed for every 1 µs-long block, by averaging the square of $Z = X + iY$ to calculate the LO phase drift [19]. After subtracting this offset, we are left with the measured symbols in X, and $Y \approx 0$. By tuning the input laser frequency and adjusting the pulse shaper parameters correspondingly to maintain equal channel amplitudes, the LO can be set to match any of the output wavelengths without altering the input data streams.

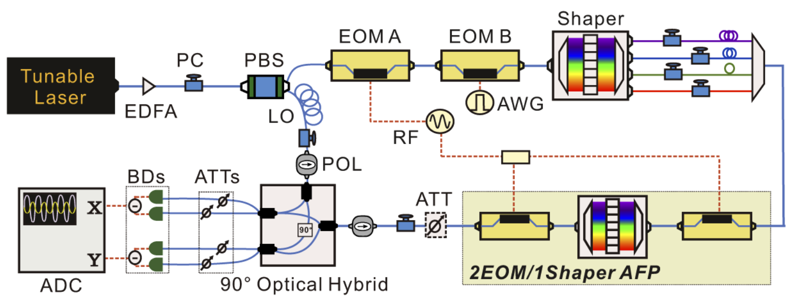

Fig. 2. Experimental setup. EDFA: erbium-doped fiber amplifier. PC: polarization controller. PBS: polarizing beamsplitter. LO: local oscillator path. POL: in-line fiber polarizer. AWG: arbitrary waveform generator. ATT: optical attenuator. BD: balanced detector. ADC: analog-to-digital converter.

The AFP's settings are found via numerical optimization, which looks for EOM/pulse-shaper parameters that maximize the SNR of the output BPSK data streams, defined for each receiver as the square of the symbol quadrature value divided by its variance (see Appendix A.1 for details on the optimization procedure). We consider a semiclassical noise model (classical fields plus LO shot noise), and take the BPSK symbol $x_n \in \{\sqrt{\mu}, -\sqrt{\mu}\}$ applied to each input wavelength channel, defined such that μ is the average photon number per symbol. Assuming the LO has frequency ω_k and (after phase correction) is aligned to measure the data originally in ω_l, the in-phase quadrature X_{kl} follows as the sum of signal, crosstalk, and noise contributions,

$$X_{kl} = K\sqrt{\eta}|V_{kl}|x_l + \sum_{n\neq l} K\sqrt{\eta}|V_{kn}|x_n \cos\beta_{kn} + d_X, \tag{4}$$

where $K = \mathcal{R}\sqrt{\mu_{\mathrm{LO}}}$ (with $\mathcal{R}$ the effective receiver response in volts/photon and μ_{LO} the LO power entering the hybrid, in units of photons per symbol), η is the overall system throughput (detector and component insertion losses for the signal channels), V_{kl} is the specific AFP transformation matrix, and β_{kn} is the phase difference between the LO and the residual signal in channel ω_k from input in ω_n. The term d_X is the noise, modeled as a zero-mean Gaussian random variable of variance $(1 + D)K^2/2$, from LO shot noise and excess detector noise D [20].

If we make the realistic assumptions of uncorrelated data streams $\langle x_k x_l\rangle = \mu\delta_{kl}$ and randomly drifting interchannel phases $\langle\cos^2\beta_{kn}\rangle = \frac{1}{2}$, then the SNR becomes

$$R_{kl} = \frac{2\mu_{\mathrm{eff}}|V_{kl}|^2}{1 + \mu_{\mathrm{eff}}\sum_{n\neq l}|V_{kn}|^2} \tag{5}$$

Optics EXPRESS

after defining an effective photon number, $\mu_{\text{eff}} = \frac{\eta\mu}{1+D}$: detected photons per symbol, normalized to shot and detector noise [12]. For any channel number N, there thus exist a total of $N \times N$ SNRs for all pairings of input and output channels, combinations of which can be used for optimization.

4. Results

We first explore 1-to-N broadcasting at $\mu_{\text{eff}} = 100$, where all N wavelengths of interest can receive the original data stream from any input channel. Hence the operation is appropriate for a single, though arbitrary, input channel transmitting at a time, in which case interchannel crosstalk terms vanish from Eq. (5), leaving $R_{kl} = 2\mu_{\text{eff}}|V_{kl}|^2$. The solver maximizes the minimum of the $N \times N$ SNR values at every iteration, i.e., $\min\{R_{00}, R_{01}, \ldots, R_{(N-1)(N-1)}\}$, which we have found more effective for yielding a uniform SNR across all channels than maximizing the SNR average [12]. (See Appendix A.1 for solutions, and measured mode transformation spectra in Appendix A.2.) The constants K, D, and $\eta\mu$ are retrieved through a calibration procedure that measures $\langle X^2 + Y^2 \rangle$ for various combinations of the LO and signal beams on and off: after attenuator adjustments, we obtain $\mu_{\text{eff}} = 102 \pm 3$, closely matched to the design of 100 and giving a baseline SNR of 204.

Figure 3 plots the experimentally obtained BPSK constellations for the broadcast operations. Since only one carrier is sent into the AFP at a time, decorrelating adjacent input channels is unnecessary, so we utilize a simple alternating data sequence. "AFP Off" gives the reference constellation, obtained for a channel passing through the AFP with the EOMs off. When the AFP is configured for either a two- or three-channel broadcast, the outputs on all wavelengths reproduce the data of the excited input channel; the SNR values and uncertainties (insets) are the mean and standard deviation of the SNRs from a 10-fold partition of the full symbol record. Good agreement with theory is obtained, which predicts SNRs of 97.5 and 60 for the two- and three-channel cases, respectively (see Appendix A.1).

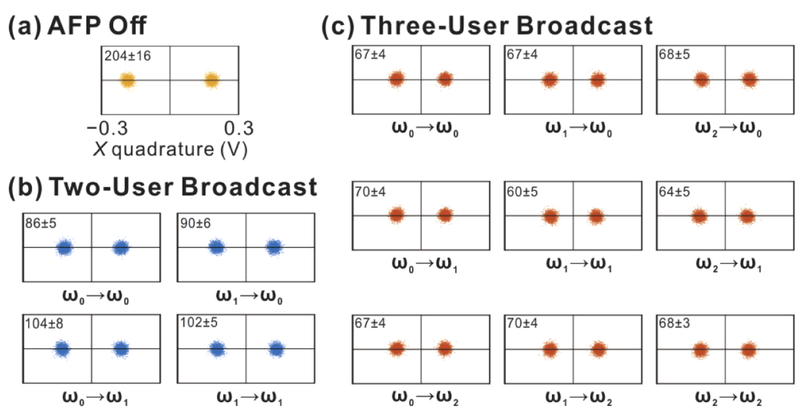

Fig. 3. Outputs for 1-to-N broadcast operations (5×10^3 symbols). (a) Reference constellation for direct throughput. The data stream is sent through the AFP with all the EOMs off (i.e., no frequency transformation). (b) Outputs for all combinations of two-user broadcasts. (c) Outputs for all three-user broadcasts. Measured SNRs follow in the insets.

As the next operation we consider cyclic frequency hopping ($\omega_0 \to \omega_1$, $\omega_1 \to \omega_2, \ldots$, $\omega_{N-1} \to \omega_0$), now at $\mu_{\text{eff}} = 1000$. This cyclic hop [12] generalizes the wavelength exchange operation explored in previous all-optical processing experiments for swapping data between two selected channels [9], by now operating on N channels simultaneously. As it can shift N inputs at the same time, we employ the full (all inputs on) SNR formula [Eq. (5)] in the design routine and optimize the metrics $\min\{R_{01}, R_{10}\}$ for $N = 2$ and $\min\{R_{02}, R_{10}, R_{21}\}$ for $N = 3$. In general,

Optics EXPRESS

frequency hopping is more challenging than broadcasting to implement on limited components [12]. For our current three-element AFP driven by a single RF tone, the output SNRs in the numerical solutions drop by ~25% and ~94% relative to the input in the two- and three-channel hops, respectively. Nevertheless, these solutions enable optimal use of available resources, and we again implement them on our AFP.

In order to test under realistic conditions of uncorrelated crosstalk, we apply a length-($2^{15}-1$) pseudorandom binary sequence (PRBS), rather than the alternating sequence used before. Our findings follow in Fig. 4. Despite the higher average photon number in this case ($\mu_{\text{eff}} = 1050 \pm 50$), the SNR of the reference signal is much lower than the theoretical value of 2000, attributable to modulation noise from our 4 GS/s arbitrary waveform generator (Tektronix AWG710) when pushing to the limits of its bandwidth (we find that the electrical SNR directly out of the machine drops by ~30 times for the PRBS compared to the alternating sequence). The expected SNRs based on a theoretical model which takes into account detection noise and crosstalk—but not this modulation noise—are 1504 and 115 for the two- and three-channel hops, respectively (see Appendix A.1). Yet since modulation noise alone (no AFP transformation) limits the optically received SNR to ~100 [Fig. 4(a)], it is expected to dominate for the $N = 2$ hop, and the SNR will be about 100, as supported by Fig. 4(b). In the case of $N = 3$, the contributions of the modulation and detection/crosstalk noise are about the same (SNRs ~100), so the expected SNR will be around 50 when combining these effects, which is likewise supported by Fig. 4(c). In this way, theory and experiment match well when considering the empirical modulation noise. Also, despite differences in received power levels for the three channels, their final SNRs remain comparable. When only one input channel is transmitted (w/o crosstalk case), the variation in hop efficiency results in SNRs that differ widely between channels. Yet when all inputs are transmitting as designed (w/crosstalk), the SNRs for the channels are equal within error, highlighting a key feature of the optimizer [12]: it balances the combination of efficiency *and* crosstalk to equalize the capacities of each channel.

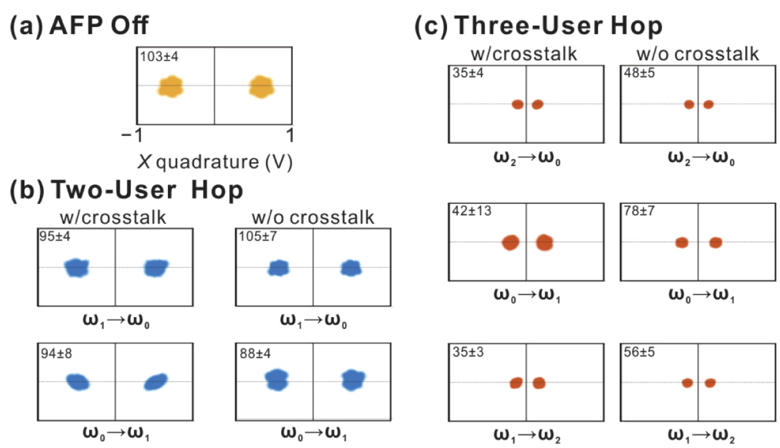

Fig. 4. Measured outputs for cyclic hop (10^6 symbols). (a) Reference constellation with AFP off. Frequency-hopped outputs for (b) $N = 2$ and (c) $N = 3$ channels. The case "w/crosstalk" corresponds to all N inputs modulated and transmitted, whereas "w/o crosstalk" to only the designated input transmitting at a time. SNR values for each plot are provided in the insets.

Optics EXPRESS

5. Discussion

While we have realized operations on up to $N = 3$ channels in the current AFP, extending beyond $N = 3$ is challenging due to our limited number of components. For example, supposing we utilize the same AFP circuit driven by single-tone sinewaves to implement a four-channel broadcasting operation and take an input SNR of 200 in channel 0, our simulations predict theoretical SNRs of 27.6, 27.6, 27.6, and 39.6 for channels 0, 1, 2, and 3 at the output—nonuniform across all channels and far below the optimal value of 50. From our previous theoretical investigations, though, scaling to much higher channel numbers should be possible with either more complex arbitrary RF modulation patterns or additional EOMs and pulse shapers; in the latter case, it appears that the number of components for near-ideal operations scales roughly linearly with channel number N [12]. This provides a straightforward path toward larger operations, with the attainable number of channels ultimately limited by the size, weight, and power budget available to the experimenter. Importantly, in contrast to the use of frequency processors in quantum information, however, the additional insertion loss associated with larger AFPs can be mitigated in the classical domain with optical amplifiers, significantly relaxing technical constraints in proceeding to larger systems. Of course, improving throughput of the AFP elements directly—which seems promising in light of advances in chip-scale EOMs [21–23] and pulse shapers [24,25]—is the ideal avenue toward larger AFPs, bypassing the additional noise and power consumption connected with optical amplification.

Another direction for improvement concerns spectral efficiency. Due to the available equipment, the present experiments considered BPSK modulation up to 1 Gb/s, but significantly faster baud rates should be supported in our system, for which advanced symbol encodings such as Nyquist pulse shaping [26–28] appear especially relevant. Based on nonoverlapping channel spectra, Nyquist encoding can reach modulation bandwidths that fill the maximum available to each wavelength, all while suppressing interchannel crosstalk as they transform through the AFP. At the spectral resolution of our pulse shaper (10 GHz intensity full-width at half-maximum), preliminary simulations suggest speeds ~10 Gbaud under Nyquist encoding should be possible with minimal degradation in SNR. And through appropriately designed high-order flattop filters [24,29,30], much sharper roll-offs than possible with diffraction-based shapers should be realizable in microring-based pulse shapers, thereby facilitating Nyquist baud rates approaching the channel spacing itself and indicating an added bonus of moving on chip. Finally, it is important to note that such limits imposed by spectral resolution are not unique to the AFP, but are shared by any WDM system employing filter-based multiplexing and measurement.

6. Conclusion

We have demonstrated agile wavelength routing functionalities using an all-optical frequency processor. The system implements broadcasting and cyclic hops for WDM channels, contributing minimal additional noise and showing good agreement with theory. Interestingly, the AFP's strengths favorably complement those of nonlinear-optical processing approaches. While the AFP offers flexibility, programmability, and precision in a variety of operations, nonlinear-optical signal processing [1] is better suited to ultrabroad bandwidths and large channel numbers, thus suggesting valuable opportunities for all-optical networking that leverage the best of both paradigms.

Appendix A. AFP transformation details

A.1. Optimization approach

To obtain an experimentally realizable AFP transformation V [Eq. (3)], we choose SNR [Eq. (5)] as our design metric, utilizing the Optimization Toolbox in MATLAB to search for an optimal set of phases for D_{EOM_1}, D_{PS}, and D_{EOM_2} that maximize the SNR values for a target operation and

Optics EXPRESS

photon level μ_{eff}. Previously [13], success probability (defined as the probability of retaining an input photon within the N frequency channels at the output, rather than scattering into adjacent channels) was adopted as the metric to optimize with quantum gate fidelity being constrained. In contrast, the usage of SNR here—like mutual information as in [12]—perfectly balances the tradeoff between fidelity (related to channel selectivity) and success probability (related to throughput) when it is impossible for both of them to reach unity given a limited amount of experimental resources. For example, when μ_{eff} is low (high), we have found the optimized solutions tend to favor better success probability (fidelity). Given practical limitations on the size of the AFP as well as the complexity of the EO modulations, we restrict the EOM patterns to single-tone sinewaves of amplitude less than 4 rad and consider a three-element AFP (EOM/pulse shaper/EOM) in all simulations. The ability to optimize settings to match the capabilities of any available system represents one of the salient features of our AFP method.

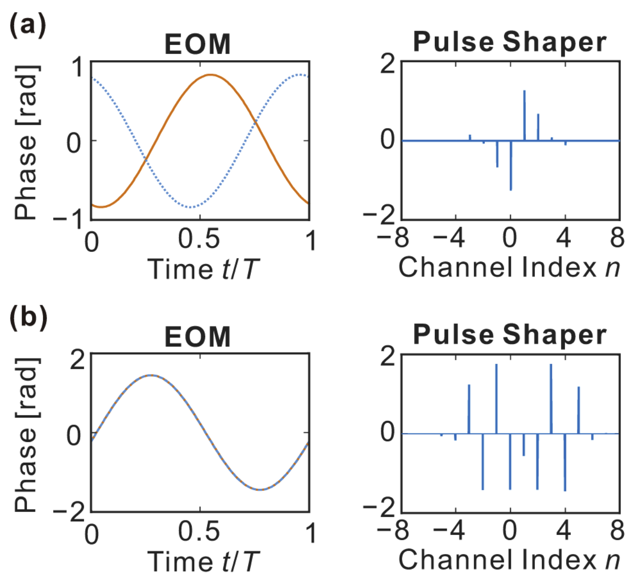

Fig. 5. Numerical solutions obtained to realize (a) two-channel and (b) three-channel broadcasts on a three-element AFP. (Left) Temporal phase modulation applied to the first EOM (solid red) and second EOM (dotted blue), plotted over one period; (Right) Spectral phase modulation programmed on the pulse shaper, where indices 0 and 1 (and 2) denote the two (three) channels of interest. Both solutions are optimized for an effective photon number $\mu_{\text{eff}} = 100$ at the input. For (b), the EO modulations are identical, and thus the two curves are on top of each other.

Here we record the specific solutions for the pulse shaper and each EOM for the two- and three-channel broadcast, designed for $\mu_{\text{eff}} = 100$. Figure 5(a) shows the results for the two-channel broadcast with a theoretical SNR of $R_{kl} = 97.5$ for all 2×2 combinations, which is close to the optimal number of ~100 ($1/N$ of the input SNR, i.e., 200 in this case, obtaining when photons are distributed equally to N channels and negligible scattering occurs outside of the network). The temporal phases on both EOMs are just phase-shifted sinewaves with a modulation depth of 0.83 rad. In addition, on the pulse shaper is programmed a spectral phase pattern wider than the total number of input channels in the network, in order to address new frequency components generated after the first EOM. The solution for the three-channel broadcast is presented in Fig. 5(b), corresponding to a theoretical SNR of $R_{kl} = 60.0$ for all 3×3 combinations. The temporal phases on the two EOMs are identical, but now the modulation depth has increased to 1.43 rad. In both broadcast designs, we are just shy of the optimal SNR values due to unwanted

Optics EXPRESS

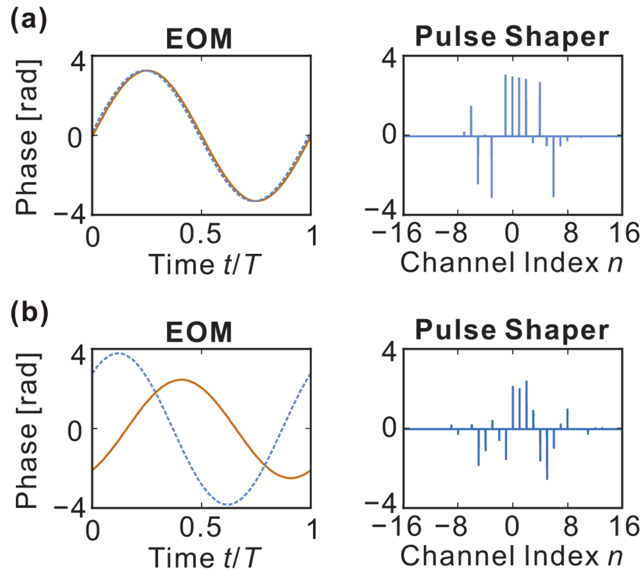

Fig. 6. Numerical solutions obtained to realize (a) two-channel and (b) three-channel hops on a three-element AFP. (Left) temporal phase modulation applied to the first EOM (solid red) and second EOM (dotted blue), plotted over one period; (Right) spectral phase modulation programmed on the pulse shaper, where indices 0 and 1 (and 2) denote the two (three) channels of interest. Both solutions are optimized for an effective photon number $\mu_{\text{eff}} = 1000$ at the input.

scattering into other frequency channels outside of the network [as shown later in Figs. 7(a) and (b) and 8(a)-(c)], which can be addressed in the future by introducing either an extra pulse shaper and EOM, or an additional RF harmonic in the EO modulation [14].

For two- and three-channel hops, we choose the input photon level $\mu_{\text{eff}} = 1000$ instead, which brings the ideal SNR to 2000 in all cases after perfect hopping operations. The optimized solution for two-channel hops is depicted in Fig. 6(a), predicting a theoretical output SNR of $R_{kl} = 1504$ for both $\omega_0 \to \omega_1$ and $\omega_1 \to \omega_0$ hops. The drop in the SNR, again, is mainly caused by photons scattering into the adjacent channels outside of the network, rather than a significant portion of the photons staying in the original channel [see Figs. 7(c) and (d)]. The EO modulations consist of slightly time-shifted sinewaves with a modulation depth of 3.26 rad. Finally, the solution for the three-channel hop is depicted in Fig. 6(b), resulting in a theoretical output SNR of $R_{kl} = 115$ for all three operations: $\omega_0 \to \omega_1$, $\omega_1 \to \omega_2$, and $\omega_2 \to \omega_0$ hops. This number is substantially lower than the ideal, suggesting that a perfect three-channel hop is markedly more difficult than the other functionalities we have addressed here. This also matches the prediction in our previous theoretical work [12], where simulations indicated considerable reduction from the ideal Shannon-limited channel capacity given fixed resources. Nevertheless, the SNR values are consistent across the three hops, and as shown in the next subsection [see Figs. 8(d)-(f)], the AFP manages to balance the effects of hop efficiency and crosstalk noise, even though they vary across all three cases.

A.2. Mode transformation spectra

Here, we show a series of input/output transformation spectra for two- and three-channel broadcast and hop, along with their theoretical prediction based on the optimized solutions obtained above. For all the results shown here, we have turned off the BPSK data stream and focus our attention

Optics EXPRESS

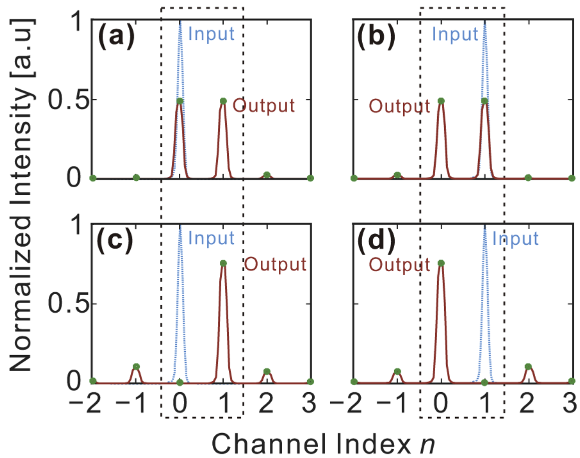

Fig. 7. Experimentally measured output spectra for (a-b) two-channel broadcast and (c-d) two-channel hop. Theoretical spectra are also plotted (green circles) for comparison. Indices 0 and 1 denote the two channels of interest in our defined WDM network (dashed box).

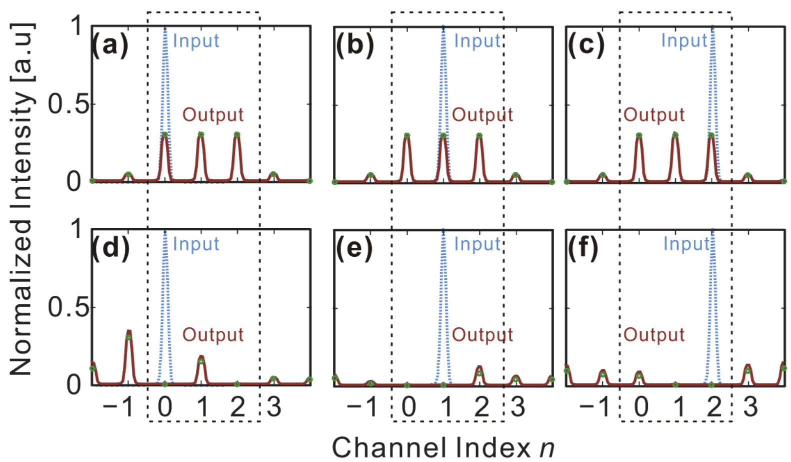

Fig. 8. Experimentally measured output spectra for (a-c) three-channel broadcast and (d-f) three-channel cyclic hop: (d) $\omega_0 \rightarrow \omega_1$, (e) $\omega_1 \rightarrow \omega_2$, and (f) $\omega_2 \rightarrow \omega_0$. Theoretical spectra are also plotted (green circles) for comparison. Indices 0, 1, and 2 denote the three channels of interest in our defined WDM network (dashed box).

solely on how the optical power in every WDM carrier is transformed into designated output channels. This procedure follows some of our previous quantum works [14,16], in which the (intensity-only) performance of a linear-optical multiport can be characterized by probing the frequency processor with a tunable, continuous-wave laser and measuring the output optical spectra.

Figure 7 shows experimentally obtained spectra for two-channel broadcast and hop: the top row shows the equi-amplitude superpositions resulting from input in either channel 0 or channel 1; the bottom row depicts the frequency hops between channels 0 and 1. For comparison, we have also plotted the theoretically predicted spectra (green dots) which show strong overlap with the experimental results, confirming the validity of the design procedure in describing practically

Optics EXPRESS

achievable systems. The small bumps in adjacent channels −1 and +2 outside of the defined network (dashed box), as discussed earlier, explain the drop in the theoretical SNR values.

Finally, the experimentally obtained spectra for three-channel broadcast and hop are recorded in Fig. 8, with the first row showing optical power splitting equally into three output channels for any one of the input channels, and the second row demonstrating the cyclic frequency hops. The amount of scattering outside of the three-channel network (dashed box) is significantly higher than that of the two-channel cases, especially the cyclic hop operation, indicating more resources are required to implement similar functionalities for a larger number of channels. Interestingly, though the mode-transformation spectra in three-channel cyclic hops [Fig. 8(d-f)] differ most significantly from the ideal scenario, they actually provide valuable insights into the interplay between the efficiency and selectivity, and how the AFP attempts to strike a balance between them in the presence of limited resources. For example, the squared-moduli of the mode-transformation matrix for the three-channel hop solution are

$$|V|^2 = \begin{pmatrix} 0.0001 & 0.0009 & 0.0595 \\ 0.1474 & 0.0024 & 0.00018 \\ 0.0011 & 0.0761 & 0.0005 \end{pmatrix}. \tag{6}$$

Although all channels, as stated earlier, attain the same theoretical SNR value of 115 at $\mu_{\text{eff}} = 1000$, their respective transformations vary greatly. For example, the ω_1 output (second row) has appreciably higher probability [Fig. 8(d)], but lower selectivity (i.e., higher crosstalk) compared to ω_0 and ω_2. The ω_0 output (first row), on the other hand, receives the lowest signals [Fig. 8(f)] among all channels, but also picks up the lowest noise. This highlights the versatility of the AFP, allowing the system to find optimal transformations and, correspondingly, higher SNR values for each channel than those possible by requiring a matrix V with elements of completely uniform amplitude [12].

Funding

Oak Ridge National Laboratory (Laboratory Directed Research and Development); U.S. Department of Energy, Office of Science, Office of Advanced Scientific Computing Research (Early Career Research Program); National Science Foundation (1839191-ECCS).

Acknowledgment

This research was performed in part at Oak Ridge National Laboratory, managed by UT-Battelle, LLC, for the U.S. Department of Energy under contract no. DE-AC05-00OR22725.

Disclosures

The authors declare no conflicts of interest.

References

1. A. E. Willner, S. Khaleghi, M. R. Chitgarha, and O. F. Yilmaz, “All-optical signal processing,” J. Lightwave Technol. **32**(4), 660–680 (2014).
2. D. A. B. Miller, “Attojoule optoelectronics for low-energy information processing and communications,” J. Lightwave Technol. **35**(3), 346–396 (2017).
3. C. Langrock, S. Kumar, J. E. McGeehan, A. E. Willner, and M. M. Fejer, “All-optical signal processing using $\chi^{(2)}$ nonlinearities in guided-wave devices,” J. Lightwave Technol. **24**(7), 2579–2592 (2006).
4. A. E. Willner, O. F. Yilmaz, J. Wang, X. Wu, A. Bogoni, L. Zhang, and S. R. Nuccio, “Optically efficient nonlinear signal processing,” IEEE J. Sel. Top. Quantum Electron. **17**(2), 320–332 (2011).
5. Q. Xu and M. Lipson, “All-optical logic based on silicon micro-ring resonators,” Opt. Express **15**(3), 924–929 (2007).

6. B. J. Eggleton, T. D. Vo, R. Pant, M. Pelusi, D. Yong Choi, S. Madden, and B. Luther-Davies, "Photonic chip based ultrafast optical processing based on high nonlinearity dispersion engineered chalcogenide waveguides," Laser Photonics Rev. **6**(1), 97–114 (2012).
7. Y. Okawachi, M. S. Bigelow, J. E. Sharping, Z. Zhu, A. Schweinsberg, D. J. Gauthier, R. W. Boyd, and A. L. Gaeta, "Tunable all-optical delays via Brillouin slow light in an optical fiber," Phys. Rev. Lett. **94**(15), 153902 (2005).
8. J. E. Sharping, Y. Okawachi, J. van Howe, C. Xu, Y. Wang, A. E. Willner, and A. L. Gaeta, "All-optical, wavelength and bandwidth preserving, pulse delay based on parametric wavelength conversion and dispersion," Opt. Express **13**(20), 7872–7877 (2005).
9. J. Wang, S. Nuccio, X. Wu, O. F. Yilmaz, L. Zhang, I. Fazal, J.-Y. Yang, Y. Yue, and A. E. Willner, "40 Gbit/s optical data exchange between wavelength-division-multiplexed channels using a periodically poled lithium niobate waveguide," Opt. Lett. **35**(7), 1067–1069 (2010).
10. C.-S. Brès, N. Alic, E. Myslivets, and S. Radic, "Scalable multicasting in one-pump parametric amplifier," J. Lightwave Technol. **27**(3), 356–363 (2009).
11. A. Biberman, B. G. Lee, A. C. Turner-Foster, M. A. Foster, M. Lipson, A. L. Gaeta, and K. Bergman, "Wavelength multicasting in silicon photonic nanowires," Opt. Express **18**(17), 18047–18055 (2010).
12. J. M. Lukens, H.-H. Lu, B. Qi, P. Lougovski, A. M. Weiner, and B. P. Williams, "All-optical frequency processor for networking applications," J. Lightwave Technol. **38**(7), 1678–1687 (2020).
13. J. M. Lukens and P. Lougovski, "Frequency-encoded photonic qubits for scalable quantum information processing," Optica **4**(1), 8–16 (2017).
14. H.-H. Lu, J. M. Lukens, N. A. Peters, O. D. Odele, D. E. Leaird, A. M. Weiner, and P. Lougovski, "Electro-optic frequency beam splitters and tritters for high-fidelity photonic quantum information processing," Phys. Rev. Lett. **120**(3), 030502 (2018).
15. H.-H. Lu, J. M. Lukens, N. A. Peters, B. P. Williams, A. M. Weiner, and P. Lougovski, "Quantum interference and correlation control of frequency-bin qubits," Optica **5**(11), 1455–1460 (2018).
16. H.-H. Lu, J. M. Lukens, B. P. Williams, P. Imany, N. A. Peters, A. M. Weiner, and P. Lougovski, "A controlled-NOT gate for frequency-bin qubits," npj Quantum Inf. **5**(1), 24 (2019).
17. H.-H. Lu, A. M. Weiner, P. Lougovski, and J. M. Lukens, "Quantum information processing with frequency-comb qudits," IEEE Photonics Technol. Lett. **31**(23), 1858–1861 (2019).
18. M. Mazur, N. K. Fontaine, H. Chen, R. Ryf, D. T. Neilson, G. Raybon, A. Adamiecki, S. Corteselli, and J. Schröder, "Multi-wavelength arbitrary waveform generation through spectro-temporal unitary transformations," arXiv:1907.02595 (2019).
19. K. Kikuchi, "Fundamentals of coherent optical fiber communications," J. Lightwave Technol. **34**(1), 157–179 (2016).
20. B. Qi, P. Lougovski, and B. P. Williams, "Characterizing photon number statistics using conjugate optical homodyne detection," Opt. Express **28**(2), 2276–2290 (2020).
21. C. Wang, M. Zhang, X. Chen, M. Bertrand, A. Shams-Ansari, S. Chandrasekhar, P. Winzer, and M. Lončar, "Integrated lithium niobate electro-optic modulators operating at CMOS-compatible voltages," Nature **562**(7725), 101–104 (2018).
22. C. Kieninger, Y. Kutuvantavida, D. L. Elder, S. Wolf, H. Zwickel, M. Blaicher, J. N. Kemal, M. Lauermann, S. Randel, W. Freude, L. R. Dalton, and C. Koos, "Ultra-high electro-optic activity demonstrated in a silicon-organic hybrid modulator," Optica **5**(6), 739–748 (2018).
23. M. He, M. Xu, Y. Ren, J. Jian, Z. Ruan, Y. Xu, S. Gao, S. Sun, X. Wen, L. Zhou, L. Liu, C. Guo, H. Chen, S. Yu, L. Liu, and X. Cai, "High-performance hybrid silicon and lithium niobate Mach–Zehnder modulators for 100 Gbit s^{-1} and beyond," Nat. Photonics **13**(5), 359–364 (2019).
24. A. Agarwal, P. Toliver, R. Menendez, S. Etemad, J. Jackel, J. Young, T. Banwell, B. E. Little, S. T. Chu, W. Chen, W. Chen, J. Hryniewicz, F. Johnson, D. Gill, O. King, R. Davidson, K. Donovan, and P. J. Delfyett, "Fully programmable ring-resonator-based integrated photonic circuit for phase coherent applications," J. Lightwave Technol. **24**(1), 77–87 (2006).
25. J. Wang, H. Shen, L. Fan, R. Wu, B. Niu, L. T. Varghese, Y. Xuan, D. E. Leaird, X. Wang, F. Gan, A. M. Weiner, and M. Qi, "Reconfigurable radio-frequency arbitrary waveforms synthesized in a silicon photonic chip," Nat. Commun. **6**(1), 5957 (2015).
26. M. Nakazawa, T. Hirooka, P. Ruan, and P. Guan, "Ultrahigh-speed 'orthogonal' TDM transmission with an optical Nyquist pulse train," Opt. Express **20**(2), 1129–1140 (2012).
27. M. A. Soto, M. Alem, M. A. Shoaie, A. Vedadi, C.-S. Brès, L. Thévenaz, and T. Schneider, "Optical sinc-shaped Nyquist pulses of exceptional quality," Nat. Commun. **4**(1), 2898 (2013).
28. J. Pfeifle, V. Brasch, M. Lauermann, Y. Yu, D. Wegner, T. Herr, K. Hartinger, P. Schindler, J. Li, D. Hillerkuss, R. Schmogrow, C. Weimann, R. Holzwarth, W. Freude, J. Leuthold, T. J. Kippenberg, and C. Koos, "Coherent terabit communications with microresonator Kerr frequency combs," Nat. Photonics **8**(5), 375–380 (2014).
29. B. Little, S. Chu, P. Absil, J. Hryniewicz, F. Johnson, F. Seiferth, D. Gill, V. Van, O. King, and M. Trakalo, "Very high-order microring resonator filters for WDM applications," IEEE Photonics Technol. Lett. **16**(10), 2263–2265 (2004).
30. F. Xia, M. Rooks, L. Sekaric, and Y. Vlasov, "Ultra-compact high order ring resonator filters using submicron silicon photonic wires for on-chip optical interconnects," Opt. Express **15**(19), 11934–11941 (2007).